

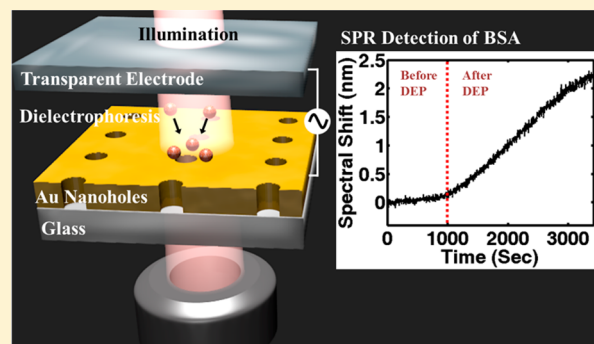
Dielectrophoresis-Enhanced Plasmonic Sensing with Gold Nanohole Arrays

Avijit Barik,^{†,‡} Lauren M. Otto,[†] Daehan Yoo,[†] Jincy Jose,[†] Timothy W. Johnson,[†] and Sang-Hyun Oh^{*,†,‡}

[†]Department of Electrical and Computer Engineering and [‡]Department of Biomedical Engineering, University of Minnesota, Minneapolis, Minnesota 55455, United States

ABSTRACT: We experimentally demonstrate dielectrophoretic concentration of biological analytes on the surface of a gold nanohole array, which concurrently acts as a nanoplasmonic sensor and gradient force generator. The combination of nanohole-enhanced dielectrophoresis, electroosmosis, and extraordinary optical transmission through the periodic gold nanohole array enables real-time label-free detection of analyte molecules in a 5 μ L droplet using concentrations as low as 1 pM within a few minutes, which is more than 1000 times faster than purely diffusion-based binding. The nanohole-based optofluidic platform demonstrated here is straightforward to construct, applicable to both charged and neutral molecules, and performs a novel function that cannot be accomplished using conventional surface plasmon resonance sensors.

KEYWORDS: Optofluidics, dielectrophoresis, nanohole array, surface plasmon resonance, plasmonics, extraordinary optical transmission, mass transport



Refractometric sensors harnessing surface plasmon resonance (SPR), charge density oscillations of conduction electrons on the metal surface, have become standard tools for measuring molecular binding kinetics and affinity.^{1–3} In SPR instruments, analytes diffuse toward and bind with receptors immobilized on the metal sensing surface. This binding interaction changes the interfacial refractive index (RI), which can be measured in real time by monitoring the SPR angle or wavelength shift.³ With continual improvements in SPR technologies, commercial instruments can detect surface coverage of proteins down to ~ 0.1 ng/cm² with bulk RI resolution of 10^{-7} refractive index units.³ However, detection of low-concentration analytes depends not only on the instrument itself but also on their transport.^{4,5} For example, assuming the detection limit of 0.1 ng/cm², purely diffusion-based detection of pM-level proteins could take many hours.⁶

To overcome this diffusion limit for surface-based biosensors, various schemes have been employed. For example, analyte binding can be accelerated by dispersing nanoparticles in a solution for rapid sampling,⁴ by electrokinetic preconcentration of charged molecules toward sensing surfaces,⁷ by utilizing evaporation-driven concentration of sample droplets,⁸ or by forcing an analyte solution through nanopores to shrink the diffusion distance.^{9–11} While integration of electrical and optofluidic manipulation schemes with SPR sensing is desirable, unpatterned gold films used in conventional SPR instruments limit our options for tailoring local electric fields and fluidic paths. In contrast, nanoplasmonic structures such as metallic nanoparticles^{12,13} or nanoholes¹⁴ open up several options to enhance SPR sensing. In particular, metallic nanohole arrays

have emerged as a versatile platform to perform SPR sensing¹⁵ as well as surface-enhanced spectroscopies,^{16,17} flow-through,^{9,10,18,19} and lipid membrane-based biosensing.^{20–23} Another attractive scheme leveraging the unique geometry of metallic nanohole arrays is dielectrophoresis (DEP)-enhanced SPR sensing, which has been proposed theoretically²⁴ but not yet shown experimentally.

Dielectrophoretic forces originate from the difference in conductivity and dielectric permittivity between an electrically polarizable particle and its surrounding medium.²⁵ External electric fields induce a net polarization at the particle-medium interface. In spatially nonuniform fields, the particle is either attracted to (positive DEP) or repelled from (negative DEP) regions of high electric field. The polarity of the DEP force and the frequency response are determined by the Clausius-Mossotti factor, $f_{CM}(\omega)$, where ω is the frequency. For a spherical particle, it is given by

$$f_{CM}(\omega) = \frac{\epsilon_p^*(\omega) - \epsilon_m^*(\omega)}{\epsilon_p^*(\omega) + 2\epsilon_m^*(\omega)} \quad (1)$$

where $\epsilon_p^*(\omega)$ and $\epsilon_m^*(\omega)$ are the complex permittivities of the particle and the medium, respectively. The time-averaged DEP force acting on a spherical particle of radius R and calculated from the electric field amplitude, E , is

Received: January 13, 2014

Revised: March 18, 2014

Published: March 19, 2014

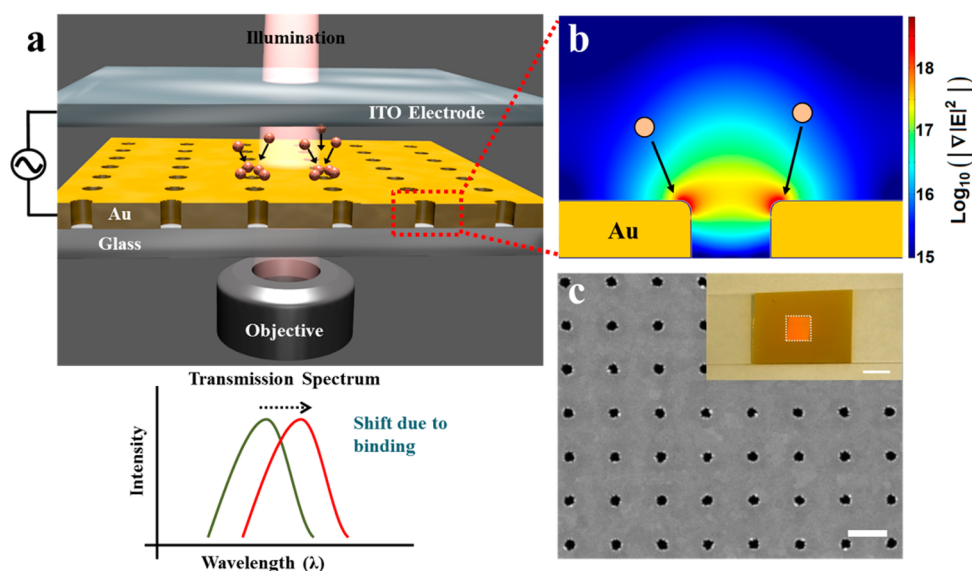


Figure 1. (a) Schematic of the experimental setup for dielectrophoretic concentration of analyte molecules. Applying suitable bias between the top indium tin oxide (ITO) electrode and gold nanohole array attracts analytes toward the gold surface. The setup was illuminated with a tungsten–halogen lamp and the transmitted light through nanohole array was collected with a 2× objective. The transmission spectrum associated with the surface plasmons at the gold–water interface shift toward longer wavelengths as the interfacial RI changes due to analyte binding. Label-free detection was performed by analyzing the spectra with an imaging spectrometer (not shown in the figure). (b) Dielectrophoretic forces attract analyte molecules toward the edge of each hole as the electric field intensity gradient is strongest (red color) along the rim of the holes. (c) SEM of the nanohole array showing a hole diameter of ~140 nm and periodicity of 600 nm. Scale bar is 500 nm. Inset: photograph of the template-stripped gold nanohole array. Scale bar is 1 cm.

$$\vec{F}_{\text{DEP}}(\omega) = \pi \varepsilon_m R^3 \text{Re}(f_{\text{CM}}(\omega)) \nabla |E|^2 \quad (2)$$

Equation 2 shows that a high electric field intensity gradient, $\nabla |E|^2$, which can be easily created in miniaturized geometries such as sharp electrode edges, metallic tips,²⁶ or micro/nanoscale gap electrodes,²⁷ can boost DEP forces. The rims of each hole in a metallic nanohole array (Figure 1) concentrate charges and thereby create strong local field gradients, thus nanohole films can concurrently act as a DEP electrode and SPR sensing substrate, which is not possible with flat gold films used in conventional SPR. Furthermore, the location of maximum plasmonic fields, that is, the rim of each hole,²⁸ coincide with the location of maximum field gradients present in DEP, thereby trapping analytes in the region of maximum detection sensitivity. Laser-illuminated metallic apertures had been previously used to trap particles via optical forces, which is also proportional to the gradient of field intensity.²⁹ Dielectrophoresis, which is based on a similar physical principle but typically occurs at radiofrequencies, is easy to implement, and can be used to attract or repel particles, thereby providing another attractive option for particle manipulation.

In this work, we integrate large-area gold nanohole arrays with a transparent electrode to experimentally demonstrate DEP-enhanced SPR sensing. Rather than using the suspended flow-through nanohole structure as proposed initially,²⁴ we choose dead-ended nanohole films, which are easier to fabricate and handle but still produce strong DEP forces suitable for molecular trapping. Transport of molecules to the sensor surface, which is normally governed by diffusion, is significantly accelerated via alternating current (ac) electric field-induced forces on the molecules. We demonstrate capture and release of 190 nm polystyrene beads on the gold nanohole surface by modulating the frequency of the applied ac signal. Finally, we detect bovine serum albumin (BSA) molecules in a 5 μL

sample droplet at 1 pM concentration owing to significantly enhanced molecular transport.

The schematic of the experimental setup is illustrated in Figure 1a. Large-area gold nanohole arrays were prepared using a combination of nanoimprinting and template stripping as described previously.^{30,31} ITO-coated glass slides (Sigma-Aldrich) were used as transparent top electrodes. The gap between the ITO-coated slide and gold nanohole array is defined by using 3M Scotch Magic tape as a spacer, whose thickness is measured to be approximately 40 μm . Binding events were monitored in real time by tracking the SPR wavelengths in the transmission spectrum. The sample solution (5 μL) was introduced into the gap and an ac signal was applied between the ITO electrode and gold nanohole array to attract analyte molecules toward the nanohole array surface (Figure 1b). A scanning electron micrograph (SEM) of the nanohole array (Figure 1c) shows a hole diameter of ~140 nm and periodicity of 600 nm. A photograph of the template-stripped gold nanohole array patterned in an area of 8 mm × 8 mm is shown as an inset to Figure 1c.

Several groups have demonstrated the SPR sensing capability of gold nanohole arrays^{15,20,32–34} based on the extraordinary optical transmission (EOT) effect.³⁵ The transmission spectrum through the nanohole array shows a series of resonant peaks and dips associated with SPR in the gold film, and these spectral features shift toward longer wavelengths as the surface-bound molecules increase the interfacial RI. For EOT-based SPR sensing, the nanohole array is illuminated with a tungsten-halogen lamp and the transmitted light collected by a 2× objective is sent to an imaging spectrometer (Newport MS257) coupled with a deep-cooled 1340 × 400 pixel CCD camera (Princeton Instruments PIXIS 400B). A MATLAB script is used to fit a polynomial function to the appropriate resonance in the spectrum and measure the resonance shift automatically.

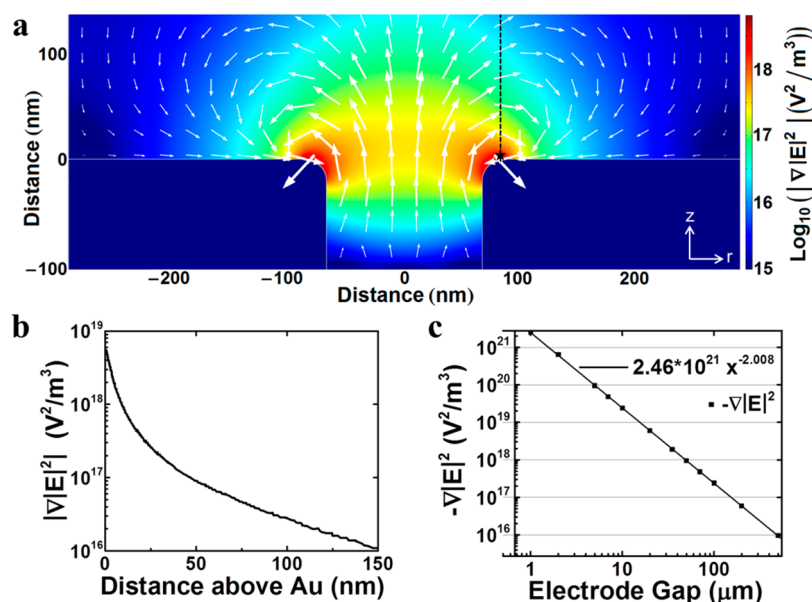


Figure 2. Finite-element method (FEM) simulations of a single 140 nm diameter nanohole in a 100 nm thick gold substrate. (a) $|\nabla E|^2$ is plotted in both magnitude (colors, logarithmically scaled) and direction (arrows, logarithmically scaled). The largest value of the magnitude of $|\nabla E|^2$ is approximately 6×10^{18} V²/m³. (b) The magnitude of $|\nabla E|^2$ plotted along the dotted line ($r = 86$ nm). (c) Dependence of the magnitude of $|\nabla E|^2$ on the distance between the ITO electrode and gold surface. Data was collected at $r = 86$ and 5 nm above the gold surface (starred).

We simulated the static electric field around a single gold nanohole (diameter of 140 and 20 nm hole edge radius of curvature) in our experimental design with a 2D axisymmetric model using FEM in COMSOL Multiphysics 4.3a. As the nanoscale features of the substrate are much smaller than the wavelength of the 1 kHz signal applied, the 6 V_{p-p} (peak-to-peak) ac was approximated as a 6 V direct current (dc) signal. A data collection point was chosen near the nanohole edge along $r = 86$ and 5 nm above the gold surface (starred in Figure 2a), which is where the radial component of the magnitude of $|\nabla E|^2$ is minimized. From eq 2, the DEP force on the particle is proportional to $|\nabla E|^2$, which is shown in both magnitude (colors, logarithmically scaled) and direction (vectors, also logarithmically scaled) in Figure 2a. Figure 2b shows the magnitude of $|\nabla E|^2$ plotted along $r = 86$ nm. The dependence of DEP force on the distance between the ITO electrode and the gold surface was determined by observing the magnitude of $|\nabla E|^2$ at the data collection point for electrode gaps, d , varying between 1 and 500 μ m and is shown in Figure 2c. A $1/d^2$ dependence was found, which matches theoretical expectations for relatively long waves interacting with a small hole in a thin sheet of metal.³⁶ Additionally, reducing the electrode gap by a factor of 3 increases the dielectrophoretic force by approximately 1 order of magnitude.

To calculate the optical field distribution on the nanohole array, three-dimensional (3D) finite-difference time-domain (FDTD) simulations were performed with a commercial software package (Fullwave, RSoft Design Group). A single 140 nm diameter hole was simulated with periodic boundary conditions along the dimensions parallel to the gold film to represent an infinite square array with a period of 600 nm. The gold film was simulated as being 100 nm thick and optical constants taken from Rakic et al.³⁷ The grid sizes in the dimensions parallel to the gold film were 3 nm while the grid in the dimension perpendicular to the gold film was 10 nm scaled down to 3 nm at the gold interface. The simulated transmission spectrum (Figure 3a) matches well with the measured spectrum

(Figure 3b). For sensing, the resonance associated with the gold–water interface was used, and Figure 3c,d shows the time-averaged electric field intensity map at the transmission maximum (856 nm) and minimum (838 nm), respectively. Previous studies have shown sensitivity to RI changes in both the transmission maximum and minimum,³⁸ and here the transmission minimum is used since it was experimentally found to be the most sensitive in our setup.

The results of dielectrophoretic manipulation of fluorescent polystyrene beads (190 nm diameter, center emission wavelength of 600 nm, Bangs Laboratories, Fishers, IN) are shown in Figure 4. For this experiment, a potential of 10 V_{p-p} was applied between the ITO electrode and the gold nanohole array, and COMSOL modeling shows an electric field strength of approximately 350 kV/m at the FEM data collection point. Polystyrene beads in a water medium (permittivity, $\epsilon_m \sim 80\epsilon_0$) of conductivity 0.28 mS/m (measured by Hach 44600) are expected to show both positive DEP and negative DEP in a frequency dependent manner as evident from the $\text{Re}[f_{\text{CM}}]$ plot shown in Figure 4b. Below the crossover frequency ($\omega = 1.67$ MHz where $\text{Re}[f_{\text{CM}}] = 0$), $\text{Re}[f_{\text{CM}}(\omega)] > 0$ and the beads are attracted toward the nanoholes, where the strength of the electric field intensity gradient is maximum. Above the crossover frequency, $\text{Re}[f_{\text{CM}}(\omega)] < 0$ and the beads are repelled away due to negative DEP. Figure 4c shows the fluorescence measurement of the entire experiment as a three-step process (2 min duration each) consisting of (i) no applied bias to establish the baseline, (ii) positive DEP with applied voltage of 10 V_{p-p} at 1 kHz, and (iii) negative DEP with applied voltage of 10 V_{p-p} at 10 MHz. Fluorescent images were recorded at regular time intervals of 10 s using a Photometrics CoolSNAP HQ2 CCD camera and Micro-Manager software. The measured fluorescence intensity (ImageJ software) over the nanohole region increases with time during the positive DEP cycle but does not return to zero during the subsequent negative DEP cycle. The residual response is due to the fluorescence from the suspended beads that are still close to the

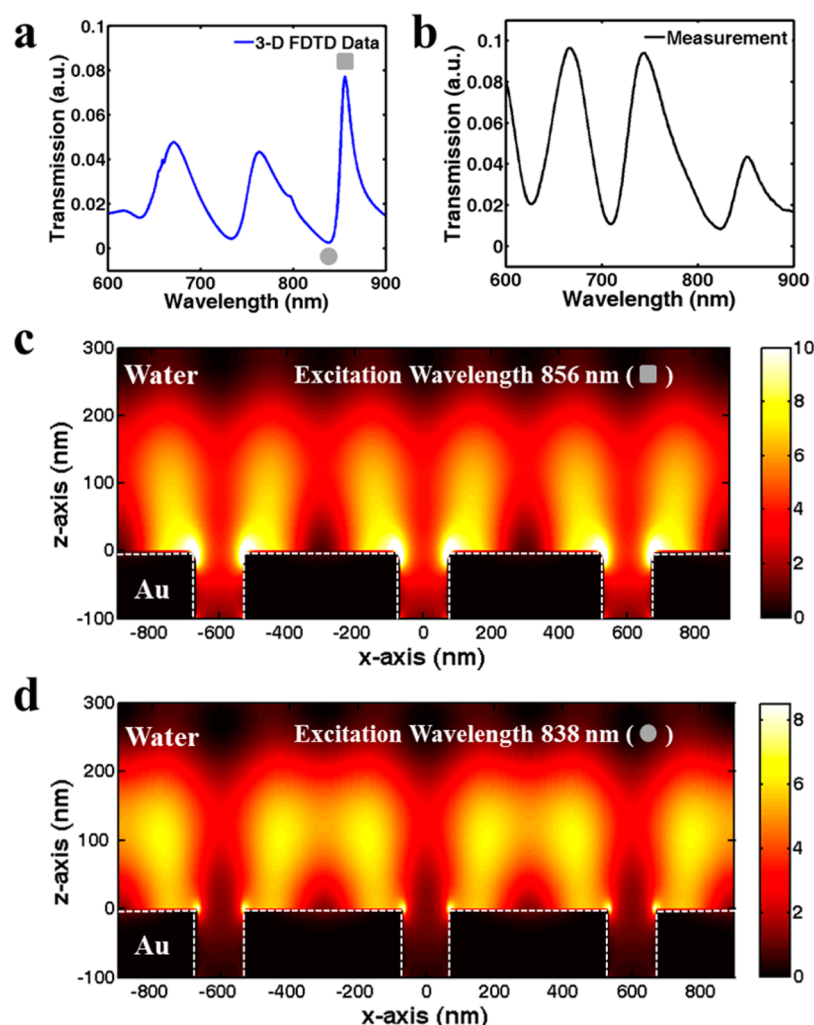


Figure 3. Three-dimensional FDTD simulations. (a) Simulated and (b) measured transmission spectra from the periodic gold nanohole arrays. The resonances associated with gold–water interface are marked. (c,d) Time-averaged electric field intensity distribution around gold nanohole arrays immersed in water at the excitation wavelengths of 856 and 838 nm, respectively.

surface but repelled from the trapping volume. In a separate experiment, we performed time-resolved SPR sensing by measuring the EOT spectrum through the nanohole array, as shown in Figure 4d. During the positive DEP cycle, the position of the minimum close to 830 nm shifts toward longer wavelengths as the beads move toward and adsorb on and around the gold nanoholes. Beads are rapidly repelled from the surface during the negative DEP cycle, as evidenced by the sudden reversal of spectral shift. In Figure 4d, we show multiple cycles of positive and negative DEP during a single experiment, demonstrating a robust reversibility. As the SPR sensing volume is much smaller than that of wide-field fluorescence imaging, background signals due to suspended beads do not contribute to the measured signal. The slight offsets in the measured spectral shift after each negative DEP cycle are attributed to a small number of beads that are immobilized on the surface by van der Waals forces.

While positive DEP trapping occurs over a wide range of frequencies, DEP force decreases rapidly as we move away from the nanoholes. Therefore, DEP force alone may not be effective in trapping molecules from the bulk solution because of the diffusion-limited transport. However, applying an electric field in a solution can also cause electrohydrodynamic effects such as joule-heating-induced electrothermal flows or ac electro-

osmosis,³⁹ which can act in concert with DEP to facilitate the transport and subsequent capture of analyte molecules on the plasmonic hotspots of the nanoholes. In our experiments, a low-conductivity solution is used to minimize any electrothermal flows,³⁹ but we do expect electroosmotic flows. In ac electroosmosis, application of an ac voltage forms an induced charge double layer at the electrode–electrolyte interface that redistributes at each cycle depending on the charge relaxation frequency of the system, given by $f = \sigma_m / (2\pi\epsilon_m)$, where σ_m is the medium conductivity.^{39,40} Electrostatic field simulation around the nanohole (Figure 2) shows a significant tangential electric field gradient that can impart a force on the double layer and generate a fluid motion via ac electroosmosis.^{40,41} Empirically, we found the most efficient frequency for trapping to be 1 kHz, which is less than the charge relaxation frequency (~ 63 kHz for $\sigma_m = 0.28$ mS/m). Thus the nanohole geometry can generate electroosmotic fluid flow and subsequently capture molecules by DEP, which is not possible to accomplish using a flat unpatterned gold film.

To demonstrate the utility of DEP-enhanced SPR sensing in detecting protein molecules at low concentrations, we used BSA (molecular weight: 65 kDa, Sigma-Aldrich) dissolved in a water medium of conductivity = 0.28 mS/m. The applied voltage was 6 V_{p-p} at 1 kHz frequency and the binding of BSA

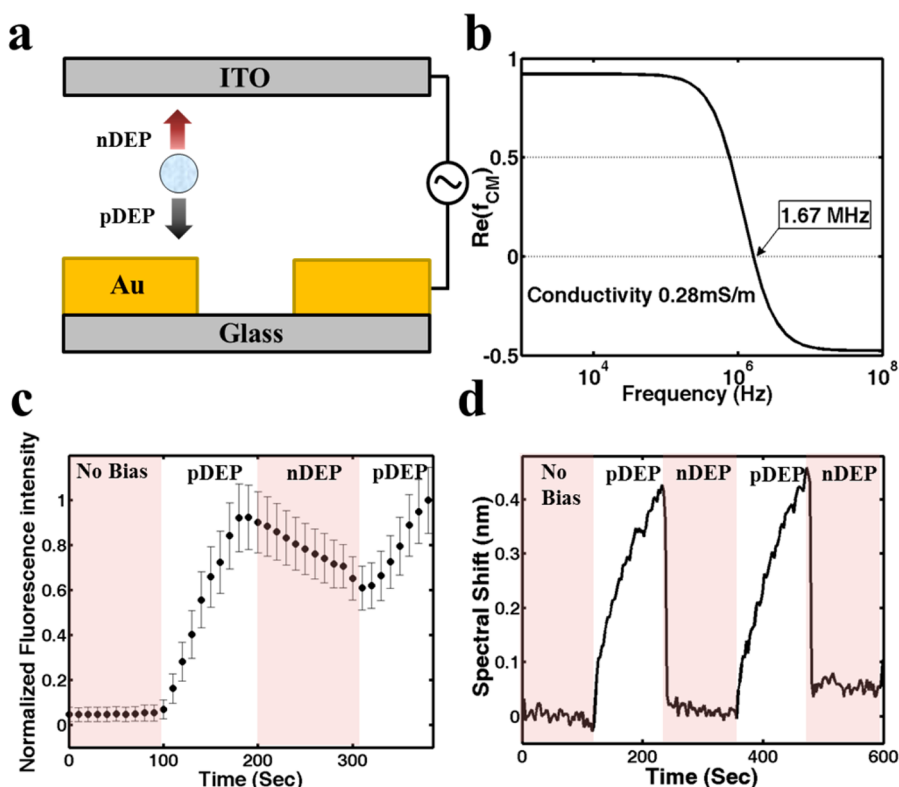


Figure 4. Dielectrophoretic manipulation of 190 nm fluorescent polystyrene beads. (a) Illustration of positive DEP (pDEP) and negative DEP (nDEP) to attract and repel the beads toward and away from the nanohole array surface, respectively. Positive DEP was carried out with applied voltage 10 V_{p-p} at a frequency of 1 kHz. For negative DEP the frequency was switched to 10 MHz. (b) Frequency dependence of the real part of Clausius-Mossotti factor (f_{CM}) for solid polystyrene beads in a suspending medium of conductivity 0.28 mS/m. (c) Normalized fluorescence intensity monitoring over a $45 \mu\text{m} \times 40 \mu\text{m}$ area of the gold nanohole array surface during positive and negative cycles of DEP. The vertical bars indicate standard deviation of each measurement. (d) Resonance shift as a function of time during repeated positive and negative cycles of DEP.

molecules on the gold nanohole array surface was monitored by recording the EOT spectrum every 2.5 s. The time-resolved spectral shifts corresponding to 1 nM, 10 pM, and 1 pM concentrations of BSA are shown in Figure 5a along with the negative control (only water). Each experiment begins with 15 min of baseline with no applied bias, followed by an ac electric field for approximately 40 min. Because of the trapping of BSA molecules on the nanohole array, spectral shifts were observed for concentrations as low as 1 pM. Furthermore, a flat line measured from the negative control experiment shows that the shift is not due to any electric field-induced fluid flow in the medium. The starting 15 min baseline also shows diffusion-based binding is negligible (Figure 5a).

In this work, we chose to investigate a medium of low conductivity, which facilitates positive DEP trapping and reduces heat generation as well as unwanted surface reactions. In solutions of higher ionic strength, we have observed irreversible spectral shifts, which is possibly due to the dissolution of the gold surface.⁴² For biological applications, it is desirable to use physiological buffer solutions, and in such cases, it may be possible to first trap molecules using DEP in a low-conductivity buffer and then inject a high-conductivity buffer for subsequent experiments.

We estimate the trapping volume of a single BSA molecule in our device by determining the threshold force

$$F_{th} = \sqrt{\frac{2}{D\Delta t}} kT \quad (3)$$

where D is the diffusion constant, Δt is the experimental time, k is the Boltzmann constant, and T is the temperature.^{43,44} For BSA trapping experiments, $\Delta t = 3300$ s and $D = 63.8 \mu\text{m}^2/\text{s}$, and the threshold force, F_{th} , is calculated to be 12.8 aN. Using eq 2 (approximating BSA as a sphere) and the volume of a BSA molecule ($\sim 163 \text{ nm}^3$),⁴⁵ we determined that the BSA trapping volume extends 30–40 nm above the nanohole edge.

We further characterized the performance of our sensor by estimating the time (time of detection, t_d) it will take to achieve limit of detection (LOD), which is defined as the concentration of analyte molecule that produces a signal corresponding to 3 times the noise level of the sensor.³ Here we compared the time of detection corresponding to each concentration of BSA with the time required for purely diffusive capture ($t_{diffusion}$) on a sensor surface. For one-dimensional diffusion of analytes in a stagnant solution, a simplified model assuming irreversible binding leads to the following equation^{46,47}

$$\Gamma(t) = 2C_{bulk} \sqrt{\frac{Dt}{\pi}} \quad (4)$$

where $\Gamma(t)$ is the surface coverage, C_{bulk} is the bulk concentration. Using eq 4, we can estimate $t_{diffusion}$ for diffusion-based SPR biosensors by measuring the time corresponding to a surface coverage value equal to the LOD of that sensor. In Figure 5b, we have shown the dependence of $t_{diffusion}$ as a function of BSA concentrations in bulk solution for a range of LOD values typical for surface-based biosensors (0.1–10 ng/cm²). For example, a sensor with LOD = 0.1 ng/cm² would take approximately 8 h to reach the detection limit

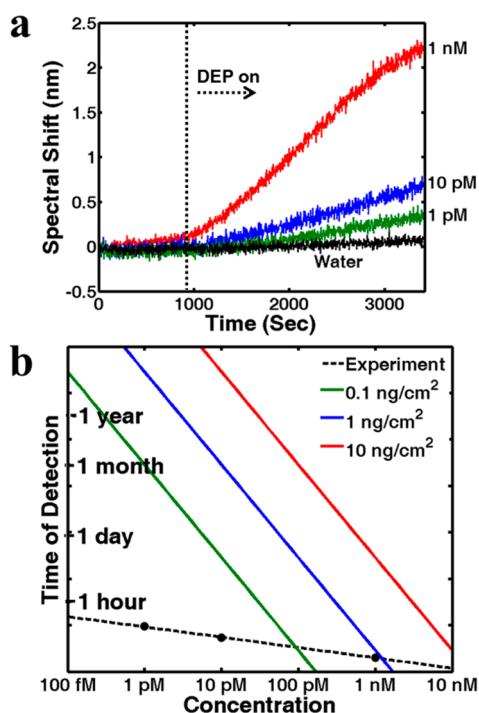


Figure 5. Low-concentration detection of BSA. (a) Time-resolved spectral shift from various concentrations of BSA (1 nM, 10 pM, and 1 pM) and control experiment (water). For these experiments a potential of 6 V_{P-P} was applied at a frequency of 1 kHz after 15 min of baseline. Measurements were taken in every 2.5 s. (b) Comparison between the time of detection for diffusion-based biosensors ($t_{\text{diffusion}}$) with typical limit of detection (0.1–10 ng/cm²) and our DEP-based experimental setup. Each dot on the plot represents t_{DEP} for different BSA concentrations. The linear fit for the experimental data shows dramatic change in the slope that enables us detection at low concentrations.

from a solution containing 10 pM BSA in a stagnant condition, whereas it only takes approximately 4 min for 100 pM BSA. This drastic difference in time of detection is due to the inverse square dependence on the bulk concentration ($t_{\text{diffusion}} \propto C_{\text{bulk}}^{-2}$), which complicates detection at ultralow concentrations (Figure 5b). Even with convection-aided analyte transport, it is challenging to detect analytes at sub-10 pM concentrations.⁶

In our experiments, t_{DEP} for each concentration was determined from the time required to achieve signal-to-noise (S/N) ratio of 3. As shown in Figure 5b, we can dramatically change the inverse square dependence in the diffusion-based model to $t_{\text{DEP}} \propto C_{\text{bulk}}^{-0.22}$ using DEP, which allows detection at low concentration within a reasonable time frame. For example, the time of detection for 10 pM BSA is approximately 8 min as compared to 8 h for diffusion limited transport, which is 60 times faster. This active dielectrophoretic concentration effect is even more pronounced at lower concentrations. For 1 pM BSA, t_{DEP} is ~14 min as compared to $t_{\text{diffusion}}$ of ~800 h; t_{DEP} is more than 1000 times faster than $t_{\text{diffusion}}$.

In conclusion, we have demonstrated efficient DEP molecular trapping and concurrent real-time SPR detection by integrating a large-area gold nanohole array with an ITO electrode. In our system, sensitive spots for SPR detection, that is, rims of gold nanoholes, coincide with the location of maximum ac electric field gradients required for DEP. The DEP-enhanced detection limit for BSA with ~1 pM concentration is significantly lower than the previous detection

limit of 100 nM for BSA using flow-through nanohole-based electrokinetic concentration.¹¹ Besides periodic nanohole arrays in metallic films, our scheme can be integrated with other nanoplasmonic sensors, such as noble metal nanoparticles,^{48,49} single isolated or random nanohole arrays,^{20,50} or flow-through nanoholes.⁹ While it is not trivial to reduce electrode gaps below 1 μm , such improvements will increase the gradient force even further and enable DEP trapping of smaller molecules at even lower concentrations. Furthermore, nanohole sensors can also function as substrates for Raman spectroscopy^{16,51} and plasmon-enhanced fluorescence detection.^{17,52,53} DEP-enhanced SPR sensors couple ultrasensitive sensors with a rapid analyte concentration technique to overcome diffusion and push the limit of detection beyond the scope of the state-of-the-art commercial systems.

AUTHOR INFORMATION

Corresponding Author

*E-mail: sang@umn.edu.

Notes

The authors declare no competing financial interest.

ACKNOWLEDGMENTS

Grants from the National Institutes of Health (NIH R01 GM092993), the National Science Foundation (NSF CAREER Award and DBI 0964216), the Office of Naval Research (ONR) Young Investigator Program, and the Minnesota Partnership Award for Biotechnology and Medical Genomics supported this work. L.M.O. acknowledges the College of Science and Engineering Fellowship from the University of Minnesota, the NIH biotechnology training grant, and the NSF Graduate Research Fellowship. T.W.J. acknowledges support from the NIH biotechnology training grant and the University of Minnesota Doctoral Dissertation Fellowship. Device fabrication was performed at the University of Minnesota Nanofabrication Center, which receives support from the NSF through the National Nanotechnology Infrastructure Network. Computational modeling was carried out in part using hardware and software provided by the University of Minnesota Supercomputing Institute.

REFERENCES

- (1) Liedberg, B.; Nylander, C.; Lundström, I. *Sens. Actuators* **1983**, *4*, 299–304.
- (2) Homola, J.; Yee, S. S.; Gauglitz, G. *Sens. Actuators, B* **1999**, *54*, 3–15.
- (3) Homola, J. *Chem. Rev.* **2008**, *108*, 462–493.
- (4) Sheehan, P. E.; Whitman, L. J. *Nano Lett.* **2005**, *5*, 803–807.
- (5) Squires, T. M.; Messinger, R. J.; Manalis, S. R. *Nat. Biotechnol.* **2008**, *26*, 417–426.
- (6) Feuz, L.; Höök, F.; Reimhult, E. *Intelligent Surfaces in Biotechnology*; Grandin, H. M., Textor, M., Eds.; Wiley: New York, 2012; Ch. 3.
- (7) Cho, H.; Lee, B.; Liu, G. L.; Agarwal, A.; Lee, L. P. *Lab Chip* **2009**, *9*, 3360–3363.
- (8) De Angelis, F.; Gentile, F.; Mecarini, F.; Das, G.; Moretti, M.; Candeloro, P.; Coluccio, M.; Cojoc, G.; Accardo, A.; Liberale, C.; Zaccaria, R. P.; Perozziello, G.; Tirinato, L.; Toma, A.; Cuda, G.; Cingolani, R.; Fabrizio, E. D. *Nat. Photonics* **2011**, *5*, 682–687.
- (9) Eftekhari, F.; Escobedo, C.; Ferreira, J.; Duan, X.; Girotto, E. M.; Brolo, A. G.; Gordon, R.; Sinton, D. *Anal. Chem.* **2009**, *81*, 4308–4311.
- (10) Jonsson, M. P.; Dahlin, A. B.; Feuz, L.; Petronis, S.; Höök, F. *Anal. Chem.* **2010**, *82*, 2087–2094.

- (11) Escobedo, C.; Brolo, A. G.; Gordon, R.; Sinton, D. *Nano Lett.* **2012**, *12*, 1592–1596.
- (12) McFarland, A. D.; Van Duyne, R. P. *Nano Lett.* **2003**, *3*, 1057–1062.
- (13) Lal, S.; Link, S.; Halas, N. J. *Nat. Photonics* **2007**, *1*, 641–648.
- (14) Brolo, A. G. *Nat. Photonics* **2012**, *6*, 709–713.
- (15) Brolo, A. G.; Gordon, R.; Leathem, B.; Kavanagh, K. L. *Langmuir* **2004**, *20*, 4813–4815.
- (16) Brolo, A. G.; Arctander, E.; Gordon, R.; Leathem, B.; Kavanagh, K. L. *Nano Lett.* **2004**, *4*, 2015–2018.
- (17) Brolo, A. G.; Kwok, S. C.; Moffitt, M. G.; Gordon, R.; Riordan, J.; Kavanagh, K. L. *J. Am. Chem. Soc.* **2005**, *127*, 14936–14941.
- (18) Yanik, A. A.; Huang, M.; Kamohara, O.; Artar, A.; Geisbert, T. W.; Connor, J. H.; Altug, H. *Nano Lett.* **2010**, *10*, 4962–4969.
- (19) Escobedo, C.; Brolo, A. G.; Gordon, R.; Sinton, D. *Anal. Chem.* **2010**, *82*, 10015–10020.
- (20) Dahlin, A. B.; Zäch, M.; Rindzevicius, T.; Käll, M.; Sutherland, D. S.; Höök, F. *J. Am. Chem. Soc.* **2005**, *127*, 5043–5048.
- (21) Jonsson, M. P.; Jönsson, P.; Dahlin, A. B.; Höök, F. *Nano Lett.* **2007**, *7*, 3462–3468.
- (22) Im, H.; Wittenberg, N. J.; Lesuffleur, A.; Lindquist, N. C.; Oh, S.-H. *Chem. Sci.* **2010**, *1*, 688–696.
- (23) Kumar, K.; Dahlin, A. B.; Sannomiya, T.; Kaufmann, S.; Isa, L.; Reimhult, E. *Nano Lett.* **2013**, *13*, 6122–6129.
- (24) Sinton, D.; Wood, P.; Escobedo, C.; Eftekhari, F.; Ferreira, J.; Brolo, A. G.; Gordon, R. *Proc. SPIE* **2009**, 7322, 732206.
- (25) Pohl, H. A. *Dielectrophoresis: The Behavior of Neutral Matter in Nonuniform Electric Fields*; Cambridge University Press: New York, 1978.
- (26) Novotny, L.; Bian, R.; Xie, X. *Phys. Rev. Lett.* **1997**, *79*, 645–648.
- (27) Krupke, R.; Hennrich, F.; von Lohneysen, H.; Kappes, M. *Science* **2003**, *301*, 344–347.
- (28) Krishnan, A.; Thio, T.; Kim, T.; Lezec, H. J.; Ebbesen, T. W.; Wolff, P.; Pendry, J. B.; Martín-Moreno, L.; García-Vidal, F. J. *Opt. Commun.* **2001**, *200*, 1–7.
- (29) Juan, M. L.; Gordon, R.; Pang, Y.; Eftekhari, F.; Quidant, R. *Nat. Phys.* **2009**, *5*, 915–919.
- (30) Nagpal, P.; Lindquist, N. C.; Oh, S.-H.; Norris, D. J. *Science* **2009**, *325*, 594–597.
- (31) Im, H.; Lee, S. H.; Wittenberg, N. J.; Johnson, T. W.; Lindquist, N. C.; Nagpal, P.; Norris, D. J.; Oh, S.-H. *ACS Nano* **2011**, *5*, 6244–6253.
- (32) Tetz, K.; Pang, L.; Fainman, Y. *Opt. Lett.* **2006**, *31*, 1528–1530.
- (33) Lesuffleur, A.; Im, H.; Lindquist, N. C.; Oh, S.-H. *Appl. Phys. Lett.* **2007**, *90*, 243110.
- (34) Yang, J.-C.; Ji, J.; Hogle, J. M.; Larson, D. N. *Nano Lett.* **2008**, *8*, 2718–2724.
- (35) Ebbesen, T. W.; Lezec, H. J.; Ghaemi, H. F.; Thio, T.; Wolff, P. *Nature* **1998**, *391*, 667–669.
- (36) Jackson, J. D. *Classical Electrodynamics*, 3rd ed.; Wiley: New York, 1998.
- (37) Rakic, A. D.; Djurišić, A. B.; Elazar, J. M.; Majewski, M. L. *Appl. Opt.* **1998**, *37*, 5271.
- (38) Sannomiya, T.; Scholder, O.; Jefimovs, K.; Hafner, C.; Dahlin, A. B. *Small* **2011**, *7*, 1653–1663.
- (39) Ramos, A.; Morgan, H.; Green, N. G.; Castellanos, A. J. *Phys. D: Appl. Phys.* **1998**, *31*, 2338–2353.
- (40) Squires, T. M. *Lab Chip* **2009**, *9*, 2477–2483.
- (41) Wu, J.; Ben, Y.; Battigelli, D.; Chang, H.-C. *Ind. Eng. Chem. Res.* **2005**, *44*, 2815–2822.
- (42) Dahlin, A. B.; Zahn, R.; Vörös, J. *Nanoscale* **2012**, *4*, 2339–2351.
- (43) Hölzel, R.; Calander, N.; Chiragwandi, Z.; Willander, M.; Bier, F. F. *Phys. Rev. Lett.* **2005**, *95*, 128102.
- (44) Morgan, H.; Green, N. G. *AC Electrokinetics: Colloids and Nanoparticles*; Research Studies Press: Hertfordshire, England, 2003.
- (45) González Flecha, F. L.; Levi, V. *Biochem. Mol. Biol. Educ.* **2003**, *31*, 319–322.
- (46) Hibbert, D. B.; Gooding, J. J.; Erokhin, P. *Langmuir* **2002**, *18*, 1770–1776.
- (47) Dahlin, A. B. *Plasmonic Biosensors: An Integrated View of Refractometric Detection*; IOS Press: Washington, DC, 2012.
- (48) Anker, J. N.; Hall, W. P.; Lyandres, O.; Shah, N. C.; Zhao, J.; Van Duyne, R. P. *Nat. Mater.* **2008**, *7*, 442–453.
- (49) Halas, N. J.; Lal, S.; Chang, W.-S.; Link, S.; Nordlander, P. *Chem. Rev.* **2011**, *111*, 3913–3961.
- (50) Rindzevicius, T.; Alaverdyan, Y.; Dahlin, A. B.; Höök, F.; Sutherland, D. S.; Käll, M. *Nano Lett.* **2005**, *5*, 2335–2339.
- (51) Lee, S. H.; Bantz, K. C.; Lindquist, N. C.; Oh, S.-H.; Haynes, C. L. *Langmuir* **2009**, *25*, 13685–13693.
- (52) Chansin, G. A. T.; Mulero, R.; Hong, J.; Kim, M. J.; deMello, A. J.; Edell, J. B. *Nano Lett.* **2007**, *7*, 2901–2906.
- (53) Miles, B. N.; Ivanov, A. P.; Wilson, K. A.; Doğan, F.; Japrun, D.; Edell, J. B. *Chem. Soc. Rev.* **2013**, *42*, 15–28.